Chapter 8: Climate Models and Their Evaluation
Figures

Coordinating Lead Authors: David Randall (USA), Richard A. Wood (UK)

Lead Authors: Sandrine Bony (France), Robert Colman (Australia), Thierry Fichefet (Belgium), John Fyfe (Canada), Vladimir Kattsov (Russia), Andrew Pitman (Australia), Jagadish Shukla (USA), Jayaraman Srinivasan (India), Ronald J. Stouffer (USA), Akimasa Sumi (Japan), Karl Taylor (USA)

Contributing Authors: K. Achuta Rao (USA), R. Allan (UK), A. Berger (Belgium), H. Blatter (Switzerland), C. Bonfils (USA, France), A. Boone (France, USA), C. Bretherton (USA), T. Broccoli (USA), V. Brovkin (Germany, Russia), W. Cai (Australia), M. Claussen (Germany), P. Dirmeyer (USA), C. Doutriaux (France), H. Drange (Norway), J.-L. Dufresne (France), S. Emori (Japan), P. Forster (UK), A. Frei (USA), A. Ganopolski (Germany), P. Gent (USA), P. Gleckler (USA), H. Goosse (Belgium), R. Graham (UK), J. Gregory (UK), R. Gudgel (USA), A. Hall (USA), S. Hallegatte (USA, France), H. Hasumi (Japan), A. Henderson-Sellers (WMO, Australia), H. Hendon (Australia), K. Hodges (UK), M. Holland (USA), A.A.M. Holtslag (The Netherlands), E. Hunke (USA), P. Huybrechts (Belgium), W. Ingram (UK), F. Joos (Switzerland), B. Kirtman (USA), S. Klein (USA), R. Koster (USA), P. Kushner (Canada), J. Lanzante (USA), M. Latif (Germany), G. Lau (USA), M. Meinshausen (USA, Germany), A.H. Monahan (Canada), J. Murphy (UK), T. Osborn (UK), T. Pavlova (Russia), V. Petoukhov(Germany), T. Phillips (USA), S. Power (Australia), S. Rahmstorf (Germany), S. Raper (UK), H. Renssen (The Netherlands), D. Rind (USA), M. Roberts (UK), A. Rosati (USA), C. Schär (Switzerland), J. Scinocca (Canada), A. Schmittner (USA, Germany), J. Scinocca (Canada), D. Seidov (USA), A.G. Slater (USA, Australia), J. Slingo (UK), D. Smith (UK), B. Soden (USA), W. Stern (USA), D. Stone (UK), K.Sudo (Japan), T. Takemura (Japan), G. Tselioudis (USA, Greece), M. Webb (UK), M. Wild (Switzerland).

Review Editors: Elisa Manzini (Italy), Taroh Matsuno (Japan), Bryant McAvaney (Australia)
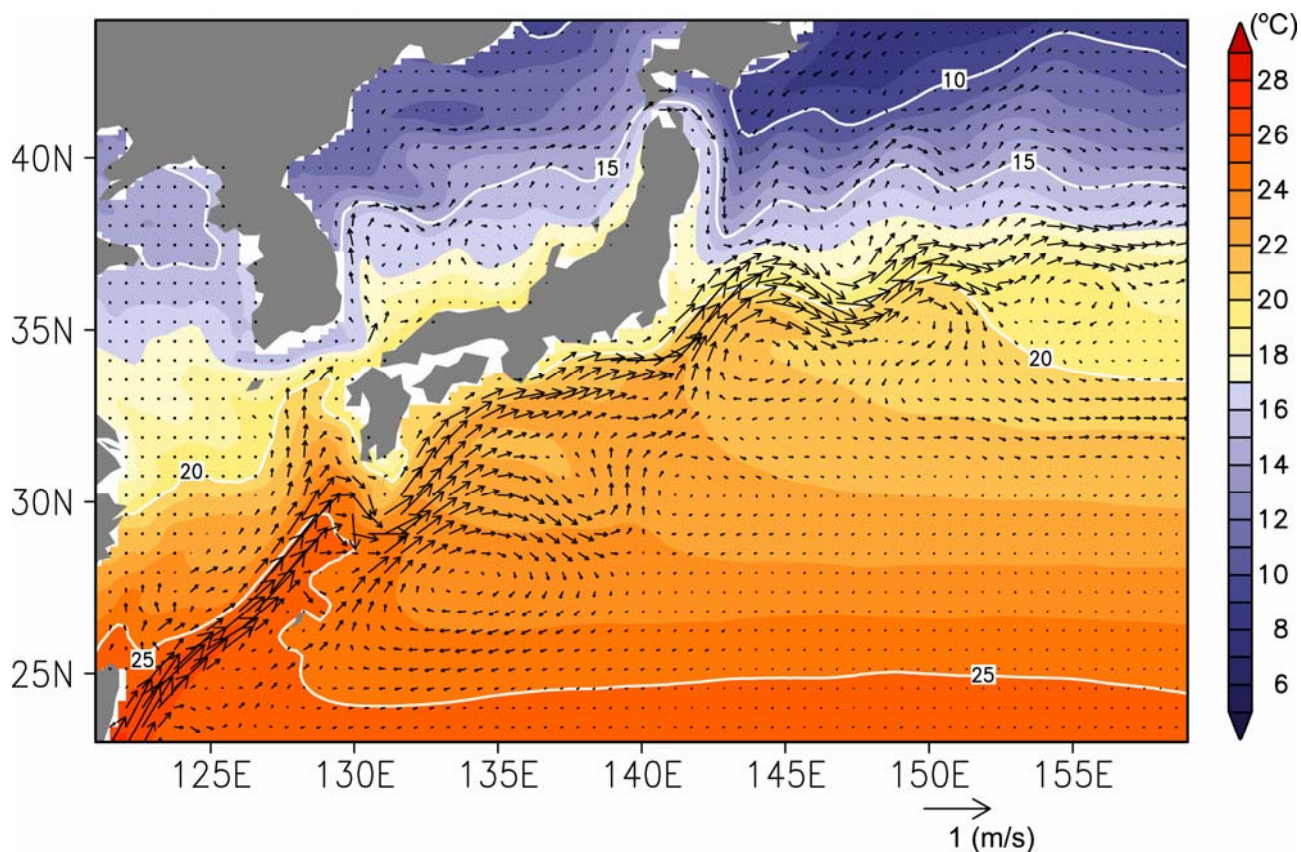
Date of Draft: 27 October 2006

1
2

3
Figure 8.1. Long-term mean ocean current velocities at 100m depth (vectors, unit: m s^{-1}) and sea surface temperature (color shades, unit: °C) around the Kuroshio and the Kuroshio Extension obtained from a control experiment which is forced by pre-industrial conditions (CO_2 concentration 295.9 ppm) using MIROC3.2_hires.
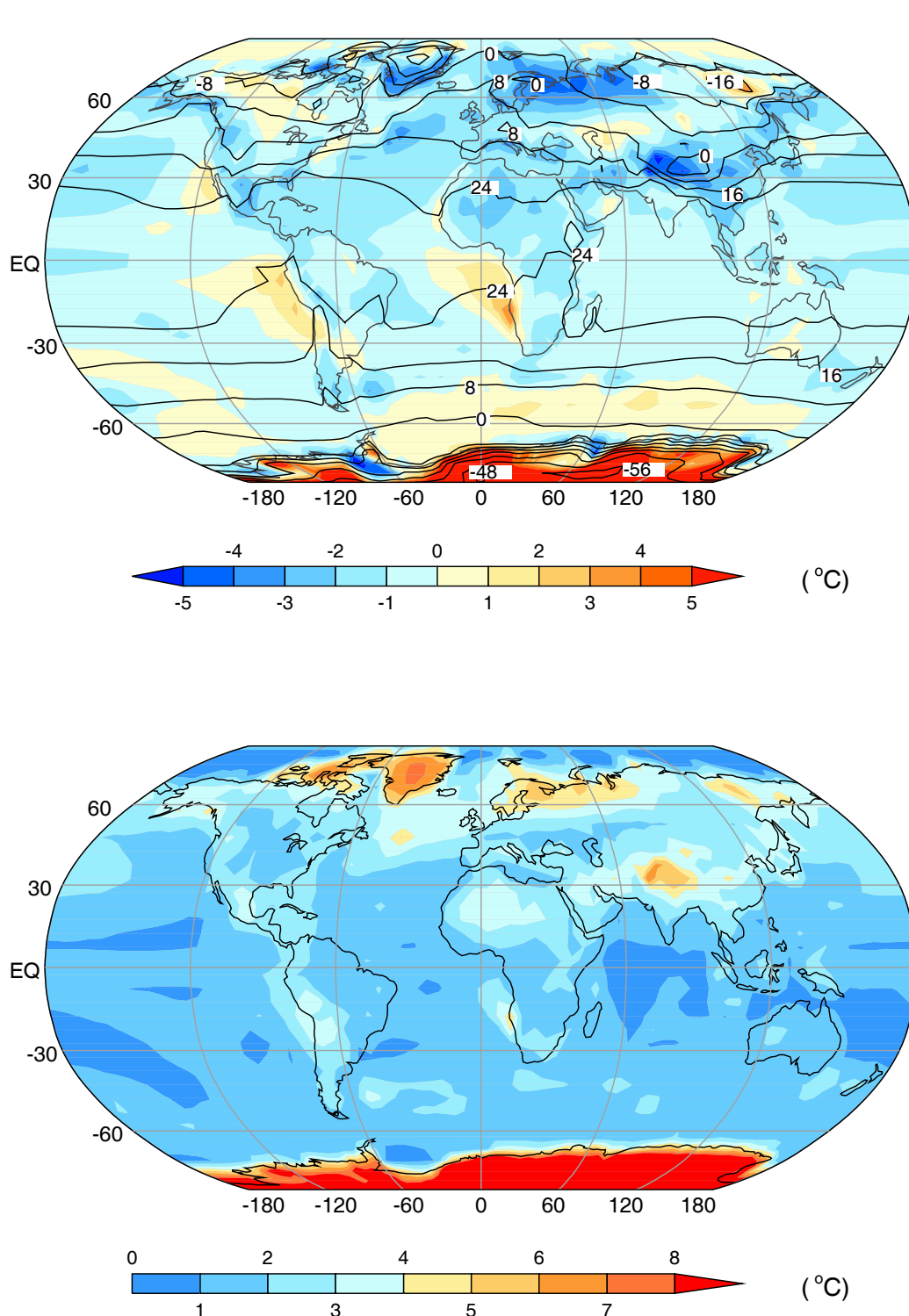8

1   **a)**

2
3
4
5
6   **b)**

7
8
9   **Figure 8.2.** Observed climatological annual-mean sea surface temperature (SST) and, over land, surface air
10   temperature (labeled contours in panel a) and the multi-model mean error in these temperatures, simulated
11   minus observed (color-shaded contours in panel a); also size of the typical model error, as gauged by the
12   root-mean-square error in this temperature (panel b), computed over all AOGCMl simulations available in
13   the multi-model dataset at PCMDI. The HadISST (Rayner et al., 2003) climatology of SST for 1980-1999
14   and the CRU (Jones et al., 1999) climatology of surface air tempeature over land for 1961–1990 are shown
15   here. The model results are for the same period of the 20th Century simulations. In the presence of sea ice,
16   the SST is assumed to be at the approximate freezing point of sea water (–1.8 °C). Temperature units are °C.
17   Results for individual models can be seen in Supplementary Material, Figure S8.1.
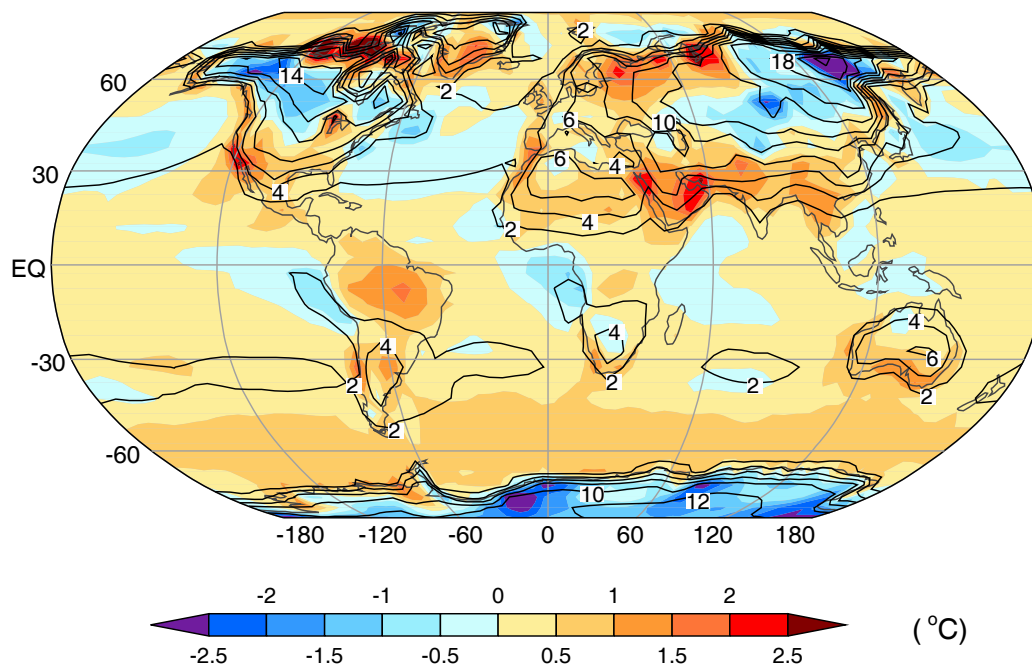18

1
2

3
4
5 **Figure 8.3.** Observed standard deviation (labeled contours) of sea surface temperature (SST) and, over land,
6 surface air temperature, computed over the climatological monthly mean annual cycle, and the multi-model
7 mean error in the standard deviations, simulated minus observed (color-shaded contours). In most regions,
8 the standard deviation provides a measure of the amplitude of the seasonal range of temperature. The
9 observational datasets, the model results, and the climatological periods are as described in Figure 8.3.1.
10 Temperature units are °C. Results for individual models can be seen in Supplementary Material, Figure S8.2.
11

1   **a)**
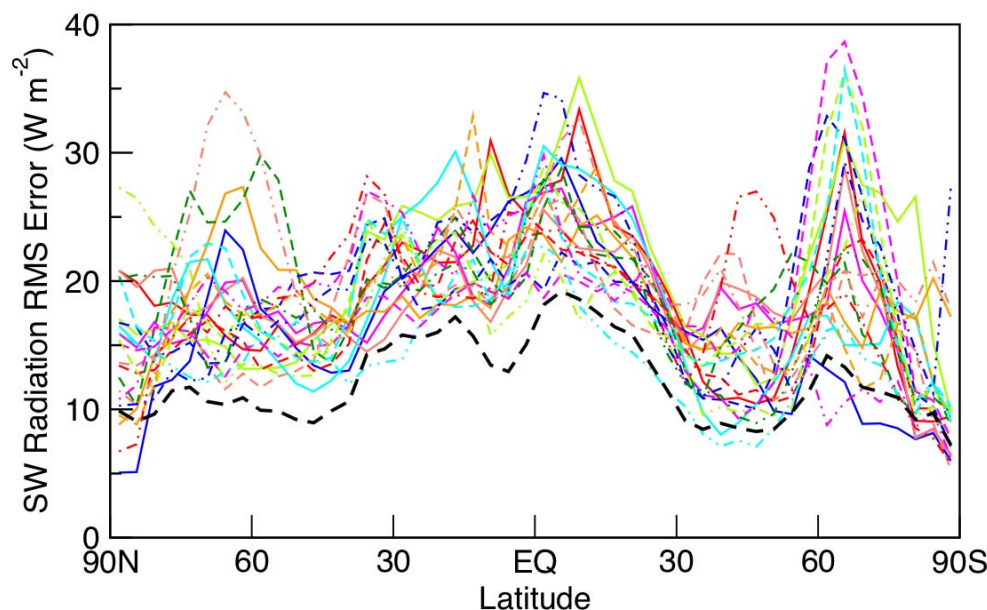
2
3   **b)**
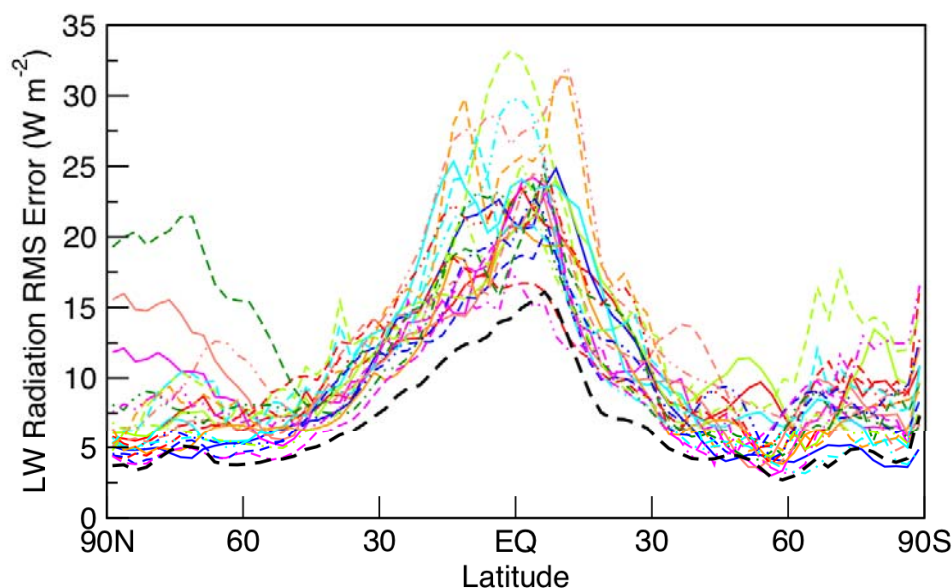
BCC-CM1	ECHO-G	IPSL-CM4
BCCR-BCM2.0	FGOALS-g1.0	MIROC3.2(hires)
CCSM3	GFDL-CM2.0	MIROC3.2(medres)
CGCM3.1(T47)	GFDL-CM2.1	MRI-CGCM2.3.2
CGCM3.1(T63)	GISS-AOM	PCM
CNRM-CM3	GISS-EH	UKMO-HadCM3
CSIRO-Mk3.0	GISS-ER	UKMO-HadGEM1
ECHAM5/MPI-OM	INM-CM3.0	"Mean Model"

4
5
6   **Figure 8.4.** Root-mean-square (RMS) model error, as a function of latitude, in simulation of: a) outgoing
7   shortwave (SW) radiation reflected to space, and b) outgoing longwave (LW) radiation. The RMS error is
8   calculated over all longitudes and over all twelve months of a climatology formed from several years of data.
9   The RMS statistic labeled "Mean Model" is computed by first calculating the multi-model monthly mean
10   fields, and then calculating the RMS error (i.e., it is *not* the mean of the individual model RMS errors). The
11   ERBE (Barkstrom et al., 1989) observational estimates shown here are from 1985–1989 satellite-based
12   radiometers, and the model results are for the same period of the 20th Century simulations in the multi-
13   model dataset at PCMDI. Results for individual models can be seen in Supplementary Material, Figures S8.5
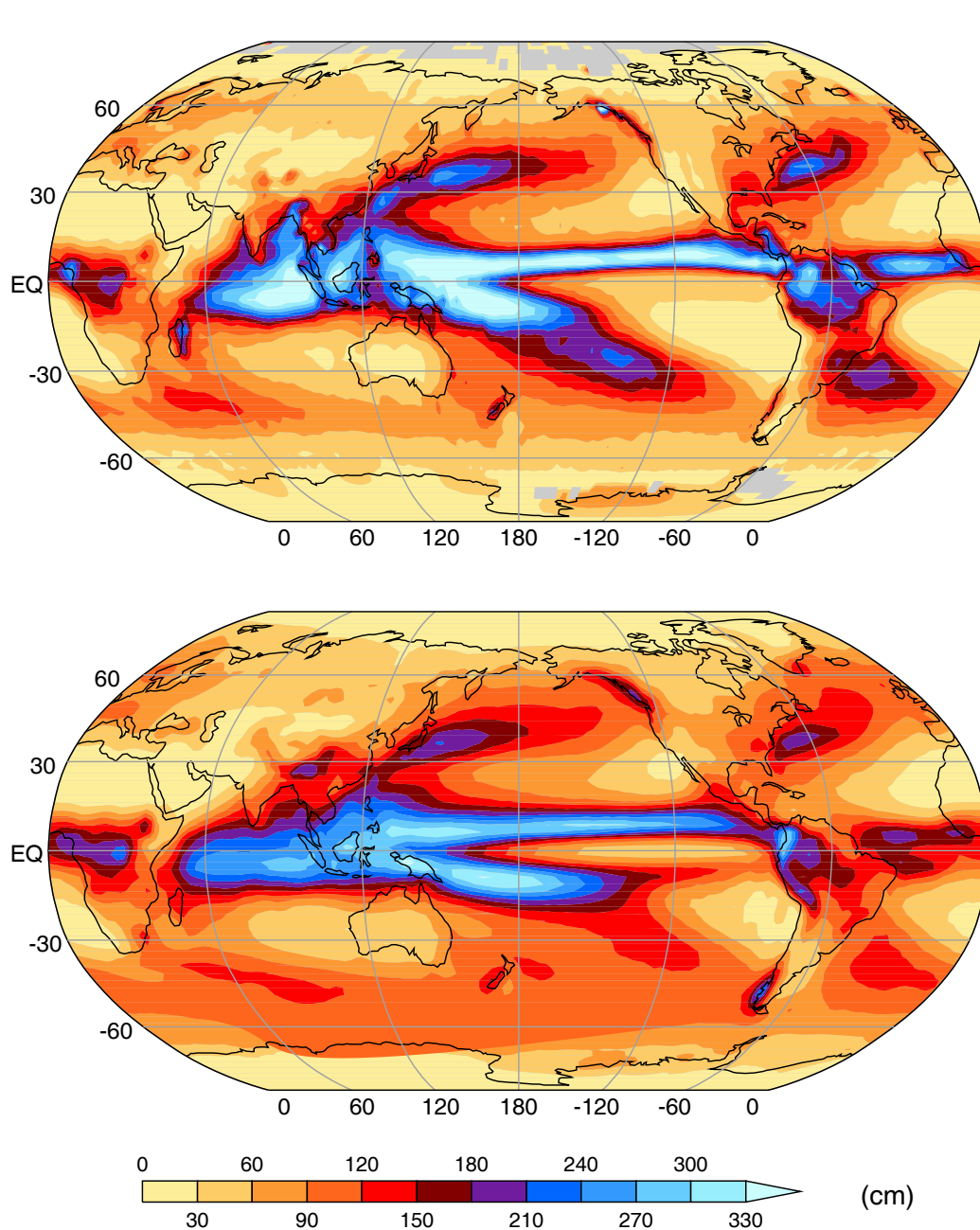14   – S8.8.

1   **a)**

b)

Figure 8.5. Annual-mean precipitation (cm), observed (panel a) and simulated (panel b), based on the multi-model mean. The CMAP (Xie and Arkin, 1997) observation-based climatology for 1980–1999 is shown, and the model results are for the same period of the 20th Century simulations in the multi-model dataset at PCMDI. In the upper panel observations were not available in the grey regions. Results for individual models can be seen in Supplementary Material, Figure S8.9.
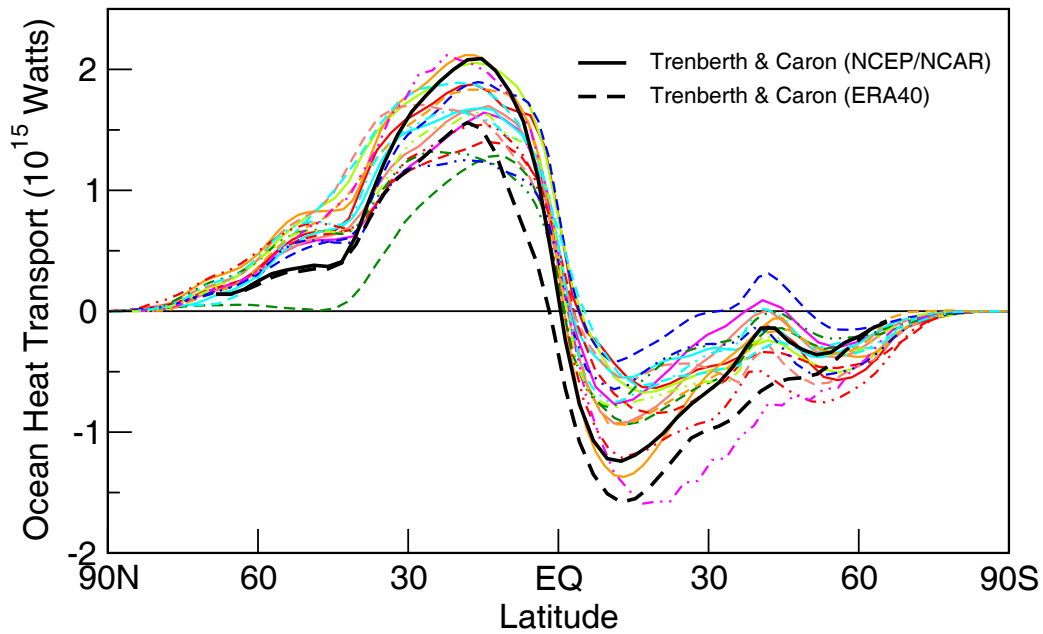
1
2

Figure 8.6. Annual-mean, zonally averaged oceanic heat transport implied by net heat flux imbalances at the sea surface, under an assumption of negligible changes in oceanic heat content. The observationally-based estimate, taken from Trenberth and Caron (2001) for the period February 1985 to April 1989, derives from reanalysis products from NCEP/NCAR (Kalnay et al., 1996) and ERA40 (Uppala et al., 2005). The model climatologies are derived from years 1980–1999 of the 20th Century simulations in the multi-model dataset at PCMDI. The legend, identifying individual models, appears in Figure 8.4.
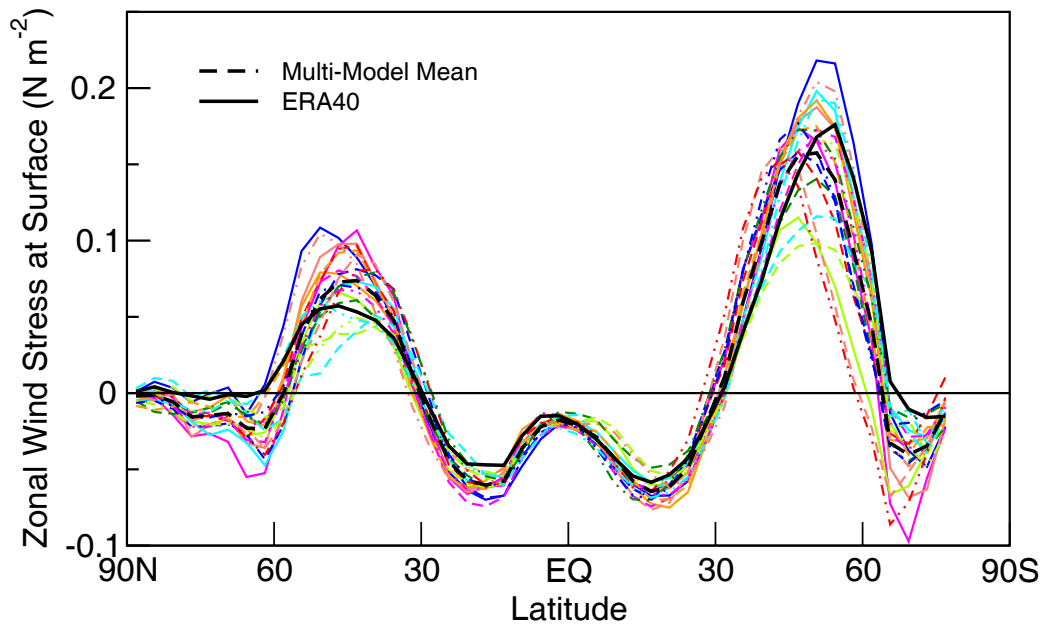
1
2

Figure 8.7. Annual-mean east-west component of wind stress, zonally averaged over the oceans. The observationally-constrained esitmate is from years 1980–1999 of the ECMWF Reanalysis (ERA40; Uppala et al., 2005), and the model climatologies are calculated for the same period of the 20th Century simulations in the multi-model dataset at PCMDI. The legend, identifying individual models, appears in Figure 8.4.
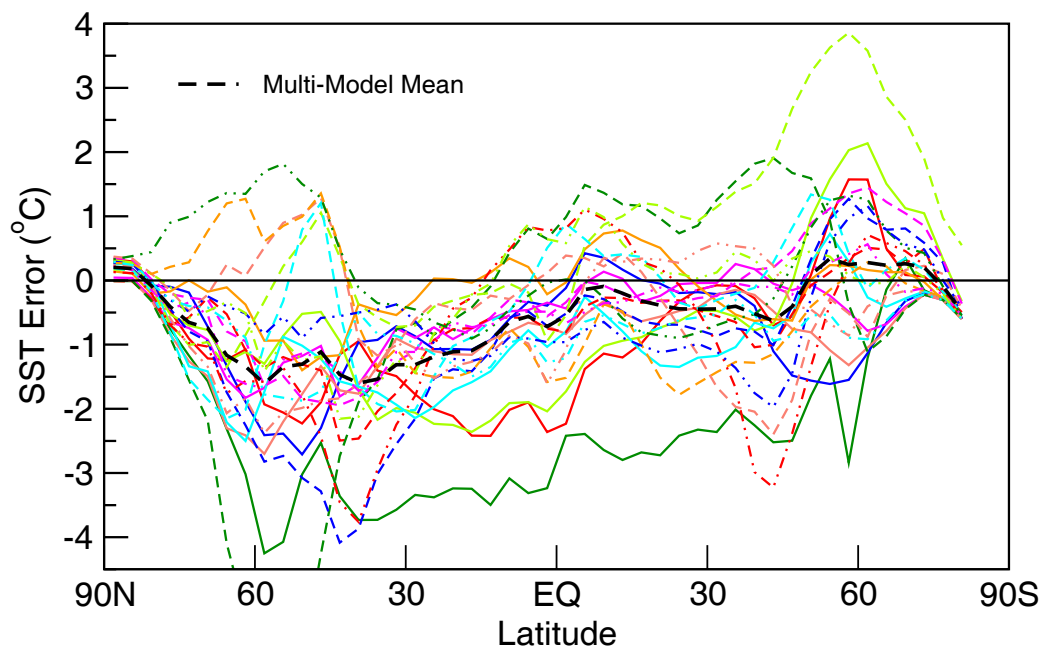
1
2

3
4
5 **Figure 8.8.** Annual-mean, zonally averaged sea surface temperature (SST) error, simulated minus observed
6 climatology. The HadISST (Rayner et al., 2003) observational climatology of 1980–1999 is the reference
7 used here, and the model results are for the same period of the 20th Century simulations in the multi-model
8 dataset at PCMDI. In the presence of sea ice, the SST is assumed to be at the freezing point of sea water. The
9 legend, identifying individual models, appears in Figure 8.4.
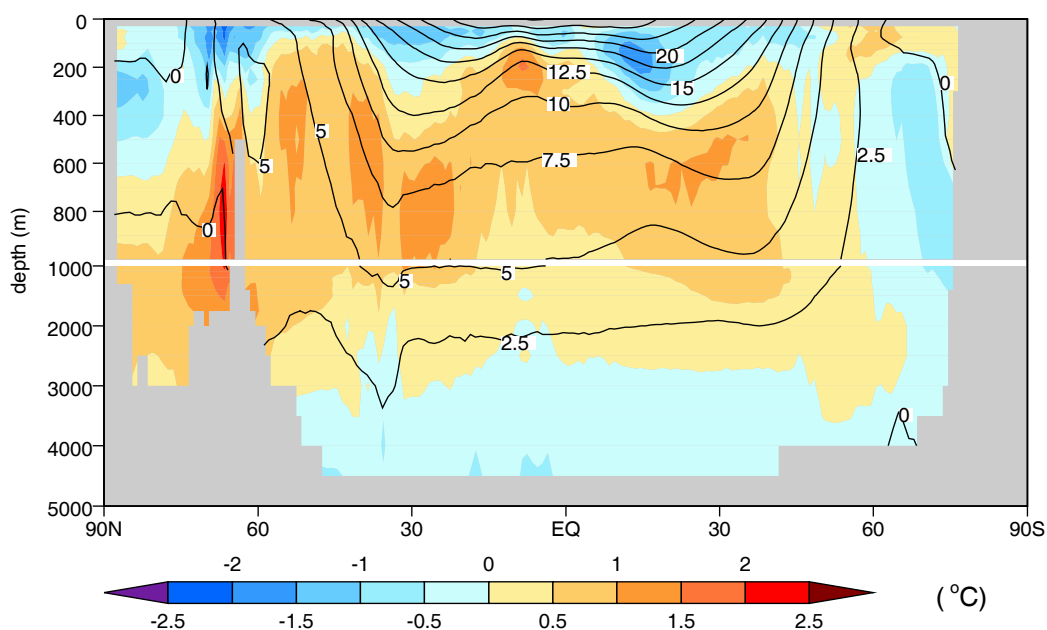10

1
2
3

4
5
Figure 8.9. Time-mean observed potential temperature, zonally averaged over all ocean basins (labeled
contours) and multi-model mean error in this field, simulated minus observed (color-filled contours). The
observations are from the 2004 World Ocean Atlas (WOA-2004) compiled by Levitus et al. (2005) for the
period 1957–1990, and the model results are for the same period of the 20th Century simulations in the
multi-model dataset at PCMDI. Temperature units are °C. Results for individual models can be seen in
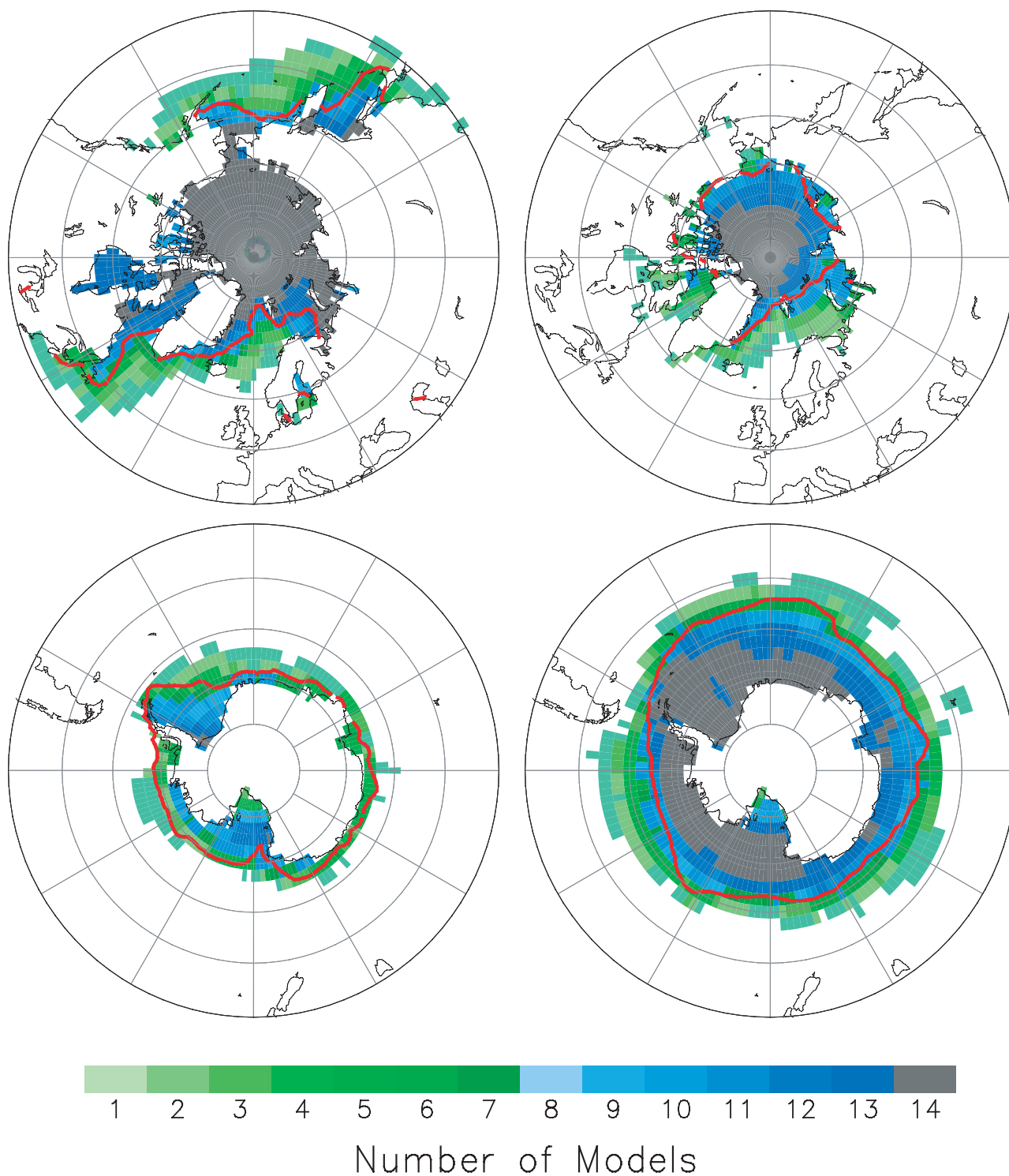Supplementary Material, Figure S8.12.

12

1
2

Figure 8.10. Baseline climate (1980–1999) sea-ice distribution in the Northern Hemisphere (upper panels)
and Southern Hemisphere (lower panels) simulated by fourteen of the AOGCMs listed in Table 8.3.1 for
March (left) and September (right), adapted from Arzel et al. (2006). For each 2.5° x 2.5° longitude-latitude
grid cell, the figure indicates the number of models that have at least 15% of the area covered by sea ice. The
observed 15%-concentration boundaries (red line) are based on HadISST (Rayner et al., 2003).

11

1
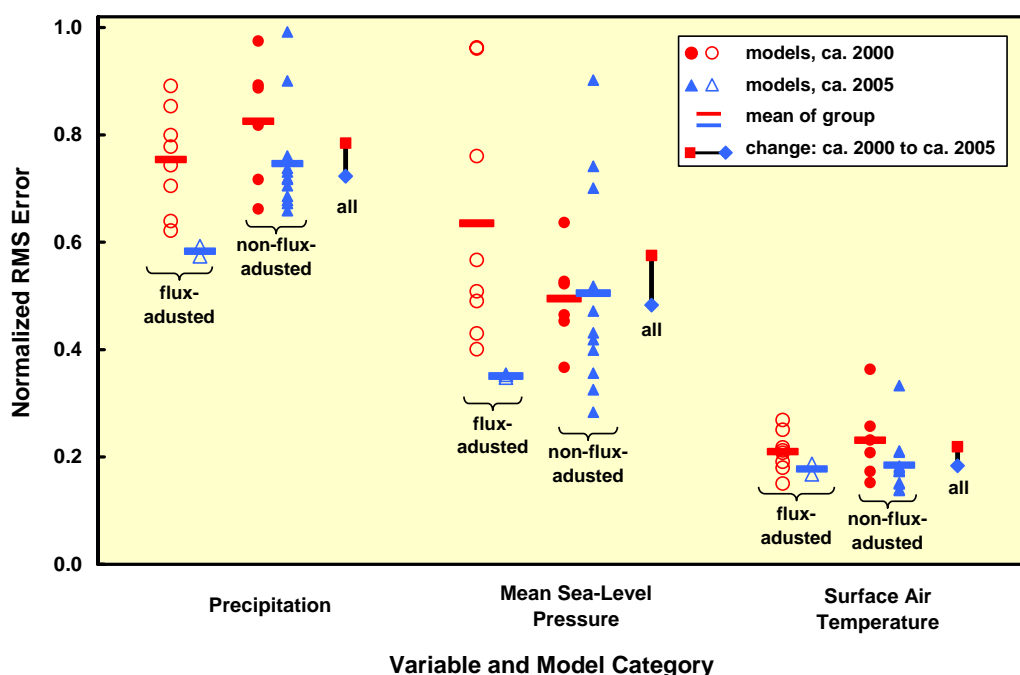
2
3
4 **Figure 8.11.** Normalized root-mean-square error in simulation of climatological patterns of monthly
5 precipitation, mean sea-level pressure, and surface air temperature. Recent AOGCMs (ca. 2005) are
6 compared to their predecessors (ca. 2000, and earlier). Models are categorized based on whether or not any
7 flux adjustments were applied. The models are gauged against the following observation-based datasets:
8 CMAP (Xie and Arkin, 1997) for precipitation (years 1980–1999), ERA40 (Uppala et al., 2005) for sea-level
9 pressure (years 1980–1999), and CRU (Jones et al., 1999) for surface temperature (years 1961–1990).
10 Before computing the errors, both the observed and simulated fields were mapped to a uniform 4 x 5 degree
11 latitude-longitude grid. For the earlier generation of models, results are based on the archived output from
12 control runs (specifically, the first 30 years, in the case of temperature, and the first 20 years for the other
13 fields), and for the recent generation models, results are based on the 20th Century simulations with
14 climatological periods selected to correspond with observations. (In both groups of models, results are
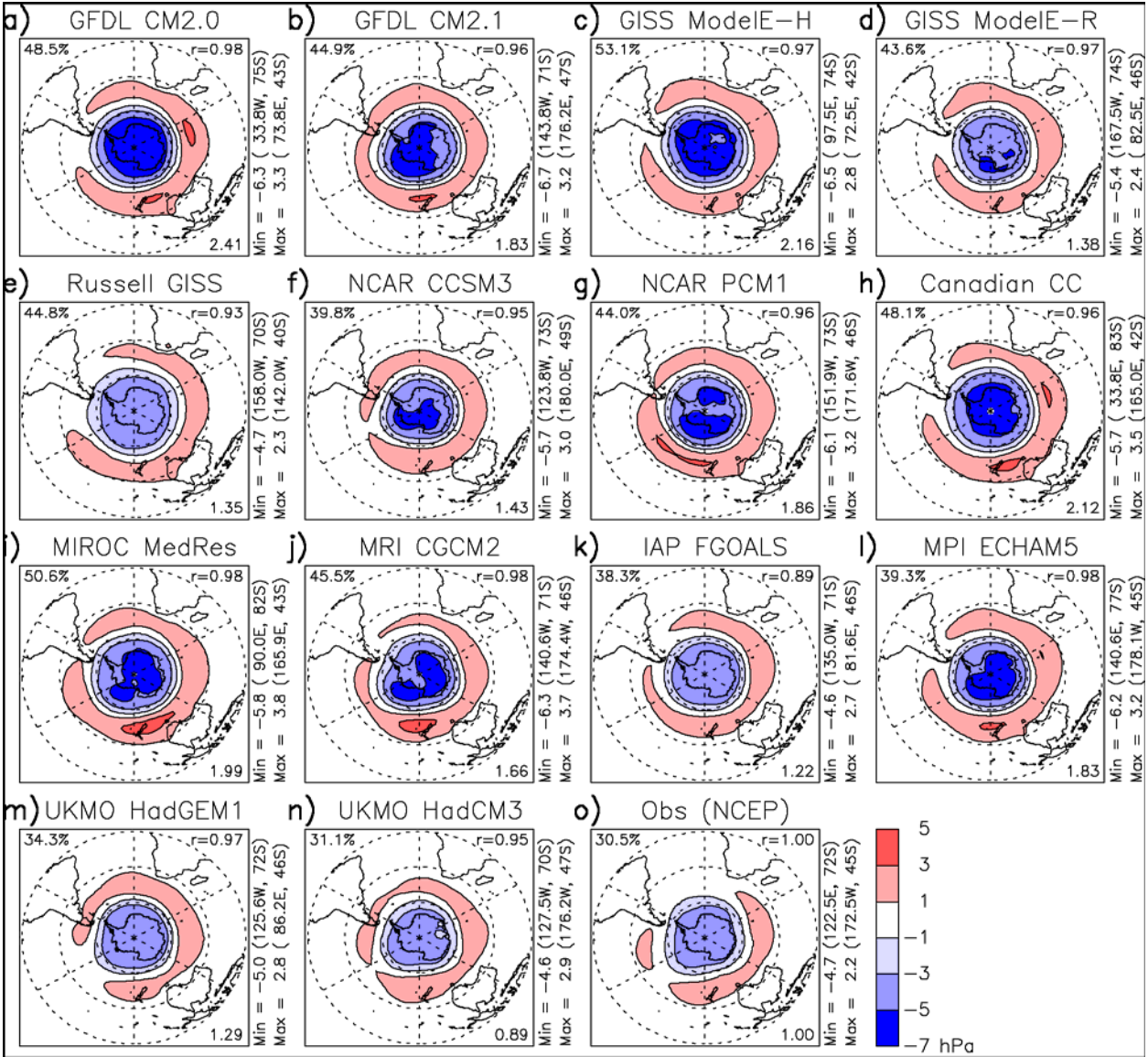15 insensitive to the period selected.)
16

1
2

3
4
5 **Figure 8.12.** Ensemble mean leading EOF of summertime (November through February) SH SLP (hPa) for
6 1950–1999. The EOFs are scaled so that the associated PC has unit variance over this period. The percentage
7 of variance accounted for by the leading mode is listed at the upper left corner of each panel. The spatial
8 correlation (*r*) with the observed pattern is given at the upper right corner. At the lower right is the ratio of
9 the EOF spatial variance of the observed value. Adapted from Miller et al. (2006).
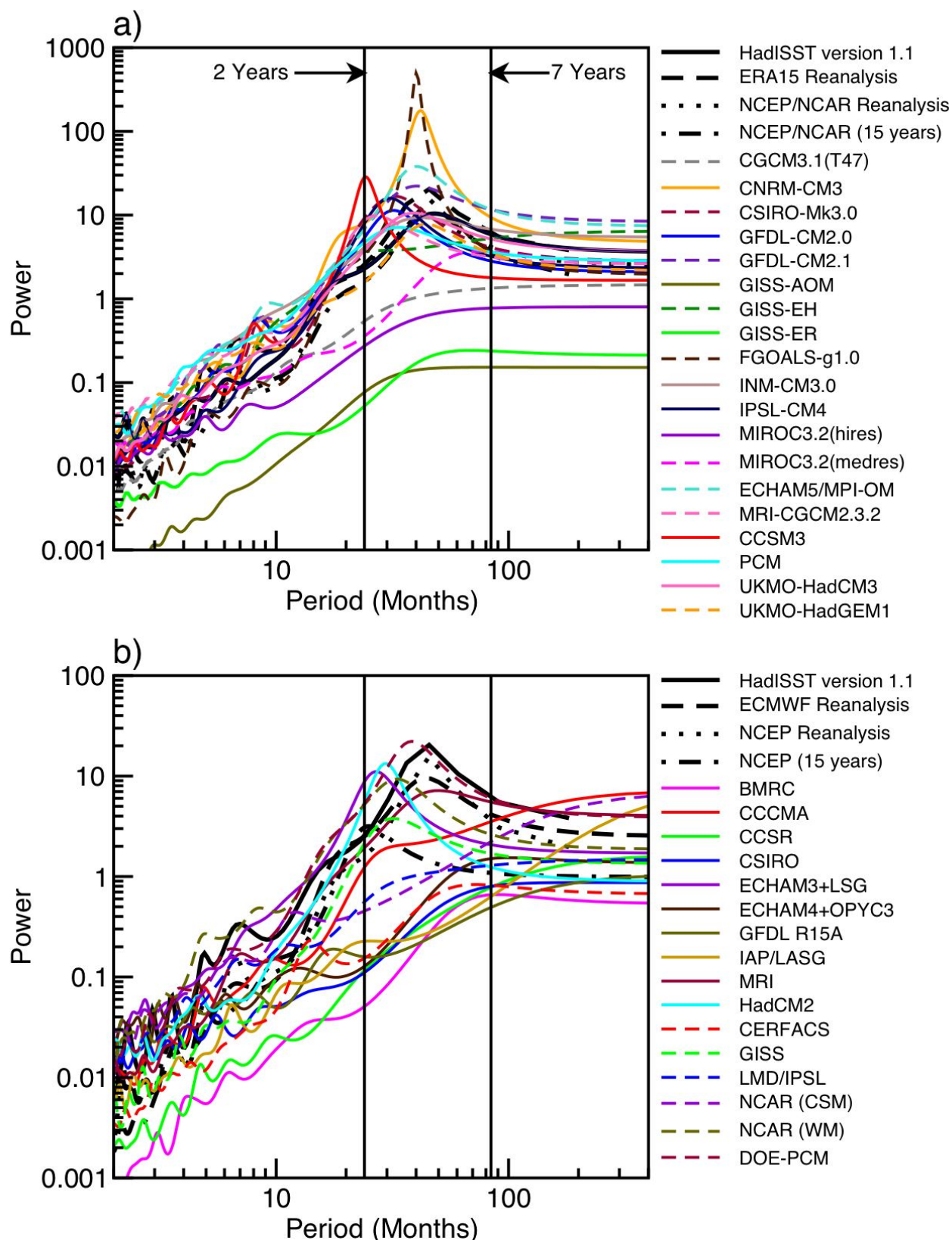10

1

Figure 8.13. Maximum entropy power spectra of NINO3 (5°N~5°S, 150°W~90° W) surface air temperature for a) the multi-model dataset at the PCMDI and b) the CMIP2 models. Note the differing scales on the vertical axes and that ECMWF Reanalysis in b) refers to the ERA15 Reanalysis as in a). The vertical lines correspond to periods of 2 and 7 years. The power spectra from the reanalyses and for SST from the HadISST version 1.1 dataset are given by the series of solid, dashed, and dotted black curves. Adapted from AchutaRao and Sperber (2006).

1
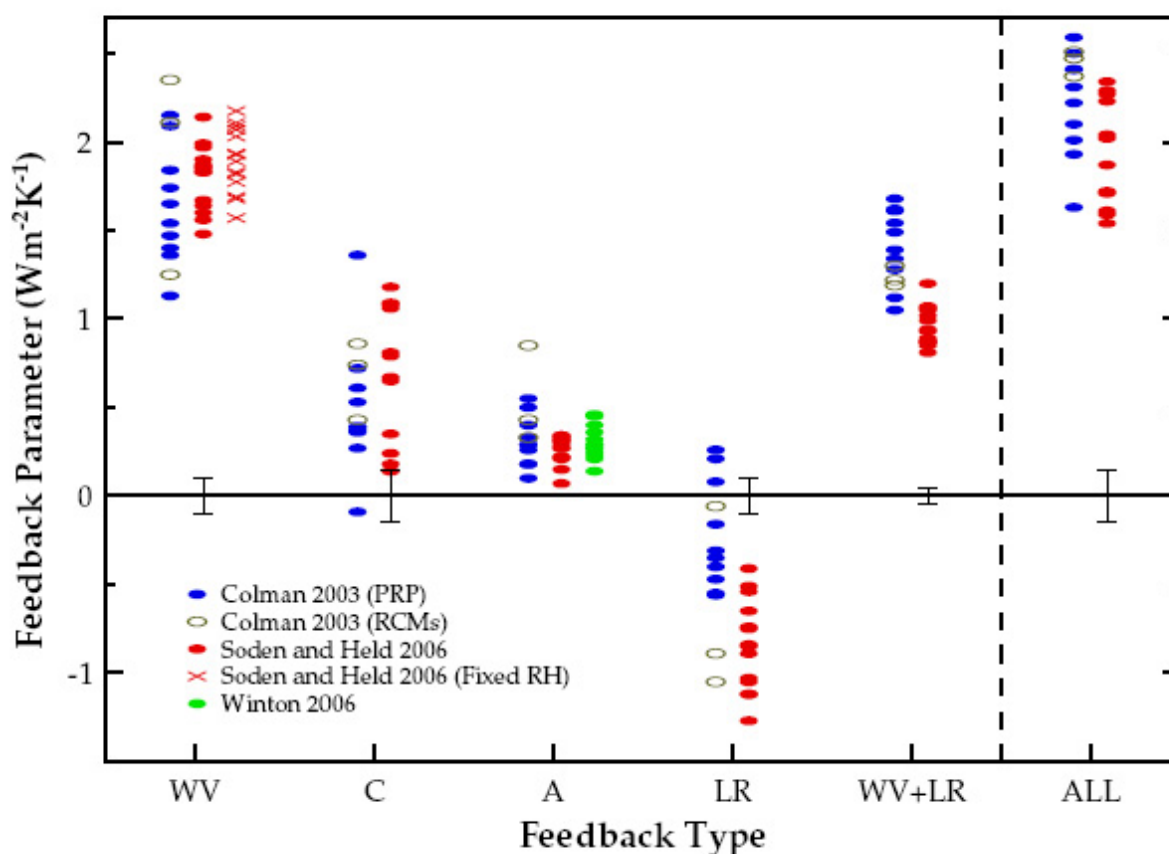
2
3
4
5 **Figure 8.14.** Comparison of GCM climate feedback parameters for water vapour (WV), cloud (C), surface
6 albedo (A), lapse rate (LR) and the combined water vapour + lapse rate (WV+LR) in units of W m^{-2} K^{-1}.
7 "ALL" represents the sum of all feedbacks. Results are taken from Colman (2003a) (blue, black), Soden and
8 Held (2006) (red) and Winton (2006a) (green). Closed blue and open black symbols from Colman (2003a)
9 represent calculations determined using the partial radiative perturbation (PRP) and the radiative-convective
10 method (RCM) approaches respectively. Crosses represent the water vapour feedback computed for each
11 model from Soden and Held (2006) assuming no change in RH. Vertical bars depict the estimated
12 uncertainty in the calculation of the feedbacks from Soden and Held (2006).
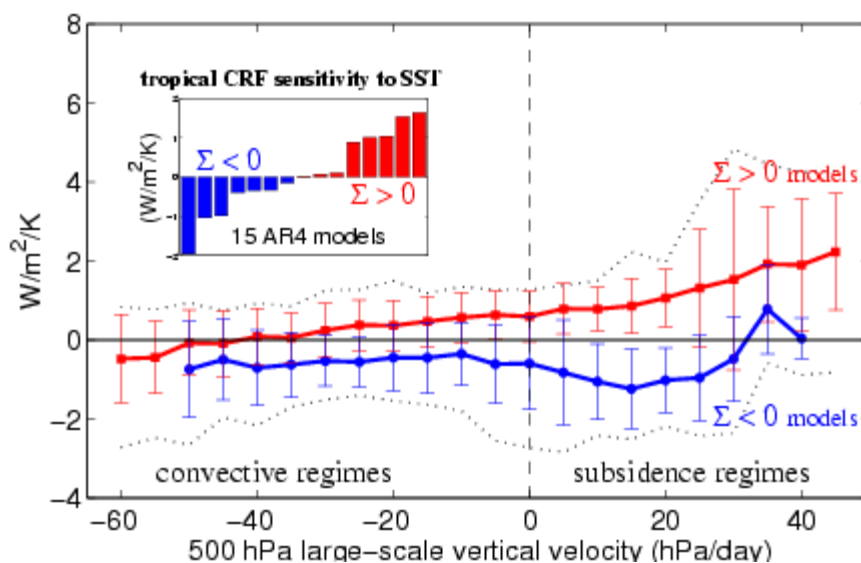13

1
2
3

4
5
6 **Figure 8.15.** Sensitivity (in W m^{-2} K^{-1}) of the tropical NET cloud radiative forcing (CRF) to sea surface
7 temperature (SST) changes associated with global warming (simulations in which CO_2 increases by 1% per
8 year). The inset shows the tropically-averaged sensitivity Σ predicted by 15 AOGCMs used in this report: 7
9 models predict $\Sigma<0$ and 8 models predict $\Sigma>0$. The main panel compares the CRF sensitivity to SST
10 predicted by the two groups of models in different regimes of the large-scale tropical circulation (the 500
11 hPa vertical pressure velocity is used as a proxy for large-scale motions, negative values corresponding to
12 large-scale ascending motions, and positive values to sinking motions).Thick lines and vertical lines
13 represent the mean and the standard deviation of model sensitivities within each group; dotted lines represent
14 the minimum and maximum values of model sensitivities within each dynamical regime.
15 The discrepancy between the two groups of models is maximum in regimes of large-scale subsidence. These
16 regimes, which have a large statistical weight in the tropics, are primarily covered by boundary-layer clouds.
17 As a result, the spread of tropical cloud feedbacks amongst the models (inset) primarily arises from inter-
18 model differences in the radiative response of low-level clouds in regimes of large-scale subsidence.
19 Adapted from Bony and Dufresne (2005).
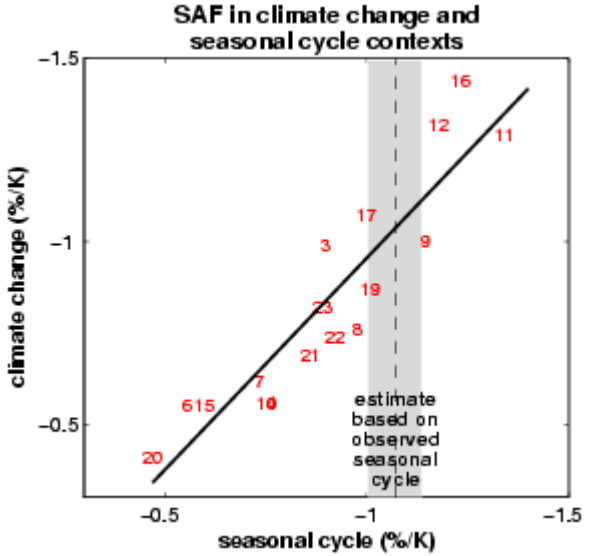20
21

1
2
3

4
5
6   **Figure 8.16.** Scatterplot of simulated springtime $\Delta\alpha_s/\Delta T_s$ values in climate change (ordinate) vs. simulated
7   springtime $\Delta\alpha_s/\Delta T_s$ values in the seasonal cycle (abscissa) in transient climate change experiments with 17
8   AOGCMs used in this report (α_s and T_s are surface albedo and surface air temperature, respectively). The
9   climate change $\Delta\alpha_s/\Delta T_s$ values are the reduction in springtime surface albedo averaged over northern
10 hemisphere (NH) continents between the 20th and 22nd centuries divided by the increase in surface air
11 temperature in the region over the same time period. Seasonal cycle $\Delta\alpha_s/\Delta T_s$ values are the difference
12 between 20th-century-mean April and May α_s averaged over NH continents divided by the difference
13 between April and May T_s averaged over the same area and time period. A least-squares fit regression line
14 for the simulations (solid line) and the observed seasonal cycle $\Delta\alpha_s/\Delta T_s$ value based on ISCCP and ERA40
15 reanalysis (dashed vertical line) are also shown. The grey bar gives an estimate of statistical error, according
16 to a standard formula for error in the estimate of the mean of a time series (in this case the observed time
17 series of $\Delta\alpha_s/\Delta T_s$) given the time series' length and variance). If this statistical error only is taken into
18 account, the probability the actual observed value lies outside the grey bar is 5%. Each number corresponds
19 to a particular AOGCM (see Table 8.1). Adapted from Hall and Qu (2006).
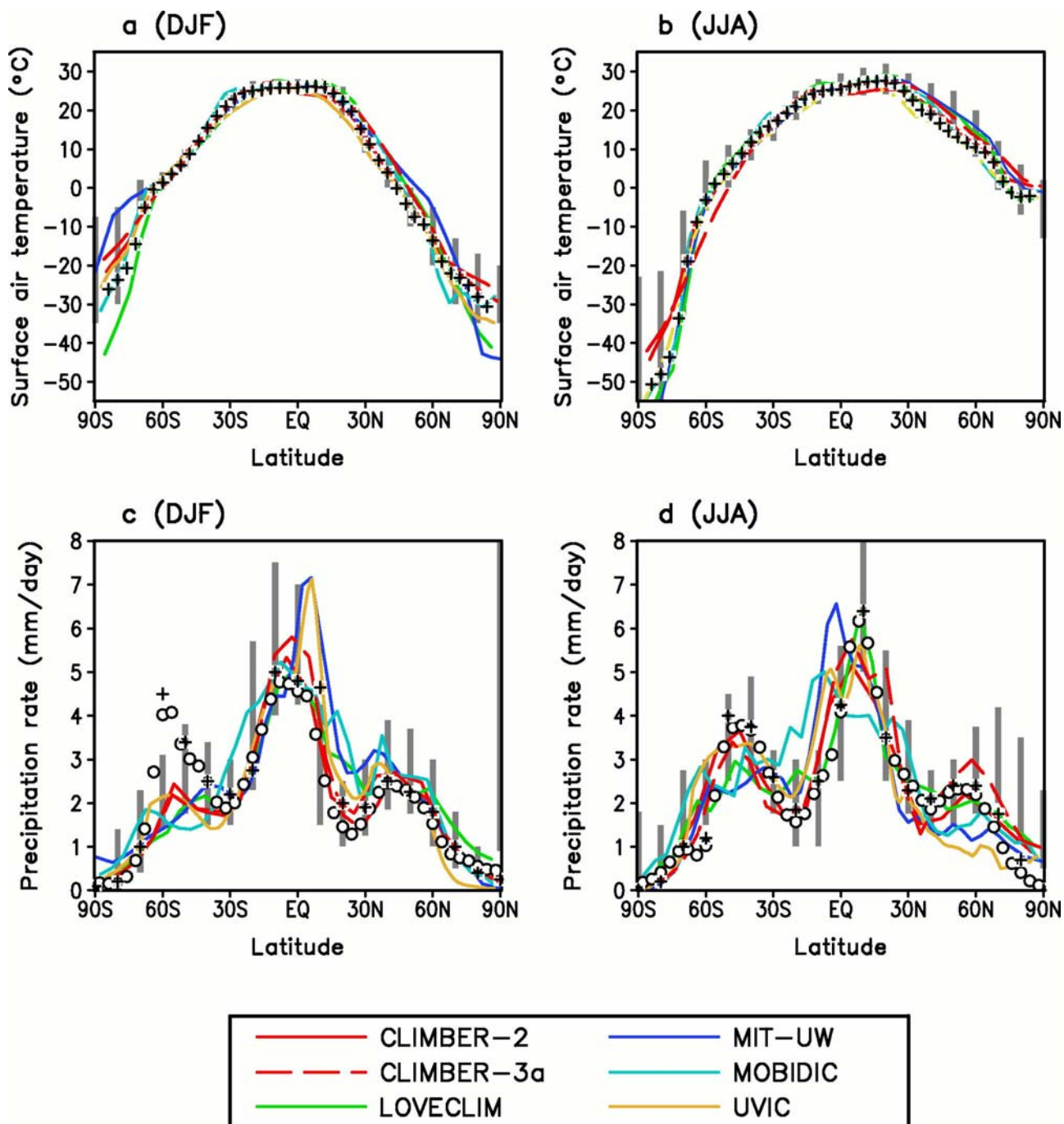20
21

1
2

3
4
Figure 8.17. Latitudinal distributions of the zonally averaged surface air temperature (a, b) and precipitation
rate (c, d) for boreal winter (December, January, February; DJF) (a, c) and boreal summer (June, July,
August; JJA) (b,d) as simulated at equilibrium by some of the EMICs used in Chapter 10 of the present
report (see Table 8.8.1) for an atmospheric CO_2 concentration of 280 ppmv. In (a) and (b), observational data
as merged from Jennings (1975), Jones (1988), Schubert et al. (1992), da Silva et al. (1994) and Fiorino
(1997) are shown by crosses. In (c) and (d), observation-based estimates from Jaeger (1976) (crosses) and
Xie and Arkin (1997) (open circles) are shown. The vertical gray bars indicate the range of GCM results
from AMIP and CMIP1 (see text). Note that the model versions used in this intercomparison have no
interactive biosphere and ice sheet components. MIT-UW is an earlier version of MIT-IGSM2.3. (Adapted
from Petoukhov et al., 2005.)

15

1
2
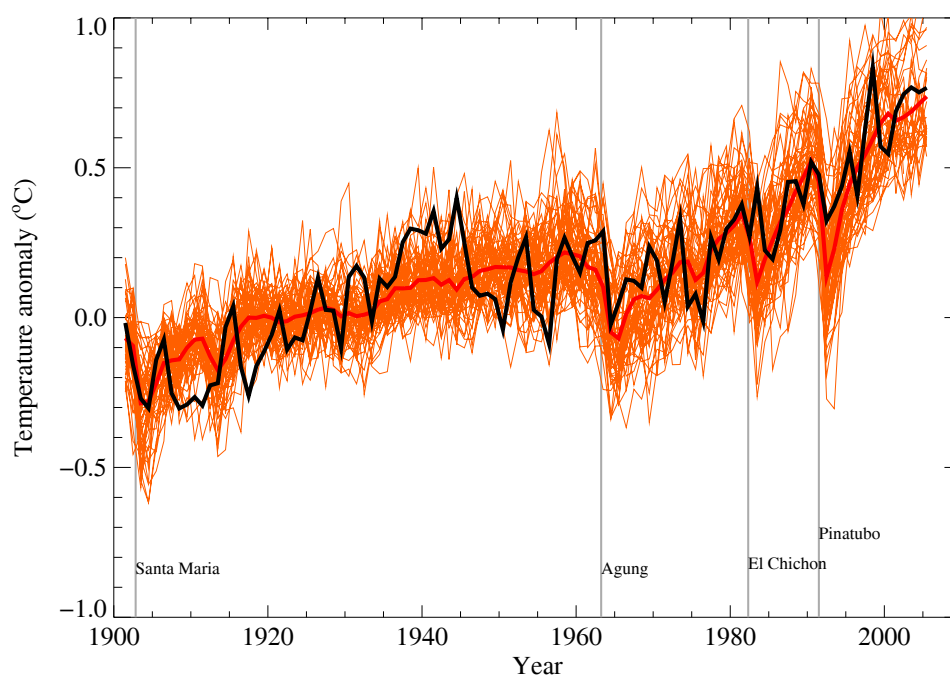
3
4
5 **FAQ 8.1, Figure 1.** Global mean near surface temperatures over the 20th century from observations (black)
6 and as obtained from 58 simulations produced by 14 different climate models driven by both natural and
7 human-caused factors that influence climate (red). The mean of all these runs is also shown (thick red line).
8 Temperature anomalies are shown relative to the 1901–1950 mean. Vertical grey lines indicate the timing of
9 major volcanic eruptions. (Figure adapted from Chapter 9, Figure 9.4.1. Refer to corresponding caption for
10 further details.)
11